Energy Advances

ROYAL SOCIETY OF CHEMISTRY

PAPER

Published on 11 August 2026

Cite this: DOI: 10.1039/d6ya00066e

A lithium-ion battery electrolyte based on dimethyl adipate and LiBOB with enhanced cycling and thermal stability

Larissa Kiefer, *[a] Chengwen Bo, [a] Philipp Finster, [b] Carlos Ziebert, [b] Andreas Hofmann, [b] Meichen Zhan [a] and Kai Peter Birke [a]

Received 6th March 2026,
Accepted 2nd August 2026

DOI: 10.1039/d6ya00066e

rsc.li/energy-advances

The thermal stability of battery electrolytes plays a decisive role in the safety and lifetime of lithium-ion cells, especially at elevated temperatures. In this work, a fluorine-free electrolyte system based on dimethyl adipate (DMA) and lithium bis(oxalato)borate (LiBOB) is developed and systematically evaluated. By combining DMA with suitable co-solvents (ethylene carbonate (EC) and propylene carbonate (PC)) while deliberately avoiding linear carbonates, electrolyte formulations suitable for operation over a wide temperature range are realized. Compared to the reference electrolyte LP40 (1 M lithium hexafluorophosphate ($LiPF_6$) in EC : diethyl carbonate (DEC) (1 : 1 wt)), the LiBOB–DMA-based electrolytes exhibit a slightly reduced initial capacity at 10 and 25 °C, consistent with increased overpotentials expected from the lower ionic conductivity. This drawback is outweighed by the markedly improved cycling stability, especially at elevated temperatures (40–60 °C), where LiBOB–DMA cells deliver higher discharge capacities from the outset and show substantially reduced degradation. At 40 °C, they retain around 95% of the initial capacity after 240 cycles, compared to 72% for LP40. Safety-relevant investigations further highlight the advantages of the LiBOB–DMA electrolyte. The DMA : EC (60 : 40 wt) solvent mixture exhibits a flash point of 135 °C, nearly 100 K higher than that of LP40. Heat–wait–seek tests in an Accelerating Rate Calorimeter (ARC) show early self-heating reactions for $LiPF_6$ -based electrolytes at around 110 °C, whereas no such behavior is observed for the LiBOB–DMA system prior to cathode decomposition. Overall, the results demonstrate the potential of LiBOB–DMA-based electrolytes for lithium-ion batteries requiring enhanced thermal safety and long-term stability.

1 Introduction

Lithium-ion batteries (LIBs) are the dominant energy storage technology for portable electronics, electric vehicles, and stationary applications due to their high energy density, long cycle life, and high efficiency. Despite these advantages, safety remains a major challenge, particularly under abusive conditions such as elevated temperatures, mechanical damage, or overcharging. In many cases, hazardous failure events originate from the electrolyte, which typically consists of flammable organic carbonate solvents combined with thermally unstable conducting salts such as lithium hexafluorophosphate ($LiPF_6$).[1–5]

State-of-the-art electrolytes are mainly based on mixtures of ethylene carbonate (EC) and linear carbonates such as diethyl carbonate (DEC) or dimethyl carbonate (DMC) with $LiPF_6$ as the conducting salt. While these electrolytes provide high ionic conductivity and good electrochemical performance, they suffer from limited thermal stability and low flash points.[1,6] Moreover, $LiPF_6$ is prone to thermal and chemical decomposition, forming PF_5 and LiF, with subsequent reactions generating HF in the presence of trace water. These species accelerate electrolyte degradation, destabilize electrode–electrolyte interfaces, and increase the risk of thermal runaway.[7–9] Given that lithium-ion cells can reach operating temperatures above 50 °C under practical conditions,[10] these limitations pose a significant safety concern.

To improve the intrinsic safety of LIB electrolytes, alternative solvent systems and conducting salts with enhanced thermal robustness have gained increasing attention. Lithium bis(oxalato)borate (LiBOB) is considered a promising alternative to $LiPF_6$ due to its higher thermal stability and its ability to form a stable solid–electrolyte interphase (SEI) on graphite anodes, even in the absence of EC.[9,11,12] Recent interest in LiBOB has further increased owing to its fluorine-free

[a] University of Stuttgart, Institute for Photovoltaics, Electrical Energy Storage Systems, Pfaffenwaldring 47, 70569 Stuttgart, Germany. E-mail: larissa.kiefer@ipv.uni-stuttgart.de
[b] Karlsruhe Institute of Technology (KIT), Institute for Applied Materials (IAM), Kaiserstraße 12, 76131 Karlsruhe, Germany

composition and its potential use in lithium-ion battery electrolytes, where it has been widely investigated as an electrolyte additive in conventional $LiPF_6$-based systems.[13–15] In addition, several studies have explored its application as a stand-alone conducting salt in LiBOB-based electrolytes.[16,17]

LiBOB also exhibits distinct moisture sensitivity compared to $LiPF_6$. Although it is not completely stable in the presence of water and can form hydrated species ($LiBOB{\cdot}xH_2O$), it shows significantly improved tolerance toward trace moisture compared to $LiPF_6$. Moreover, its hydrolysis products are considerably less reactive and less corrosive than those of $LiPF_6$, which readily generates highly reactive species upon decomposition.[9,18–20]

Beyond LiBOB, several other fluorine-free lithium salts have been explored. Lithium perchlorate ($LiClO_4$) was previously used due to its high solubility and ionic conductivity but is now largely avoided because of its strong oxidizing nature and safety concerns.[19,20] Phosphate-based salts such as lithium tris(oxalato) phosphate (LiTOP) and lithium tris[1,2-benzenediolato(2-)-O,O′]phosphate (LiTBP) have also been proposed, although LiTOP remains at an early stage of development and LiTBP is limited by a relatively low electrochemical stability window (<3.7 V *vs.* Li/Li^+), restricting high-voltage applications.[19,20] Lithium nitrate ($LiNO_3$) offers advantageous SEI-forming capability and high stability but suffers from poor solubility in organic solvents. Other boron-based salts, such as lithium bis(malonato)borate (LiBMB) and lithium (malonatooxalato)borate (LiMOB), show stronger Li^+ coordination than LiBOB, leading to reduced dissociation and lower ionic conductivity. In comparison, LiBOB provides a favorable balance of thermal stability, safety, electrochemical performance and environmental compatibility.[19,20] However, LiBOB generally exhibits lower solubility and ionic conductivity in conventional carbonate solvents compared to $LiPF_6$,[21–23] which necessitates careful electrolyte design and optimization.

In parallel, the use of high-boiling, low-volatility ester-based solvents has emerged as an effective strategy to enhance electrolyte safety.[24] In this study, dimethyl adipate (DMA) is investigated as a non-fluorinated and potentially less hazardous electrolyte solvent in combination with LiBOB as the conducting salt. DMA is a linear diester characterized by a high boiling point, low vapor pressure, and a significantly higher flash point compared to commonly used linear carbonates.[25–28] These physical properties make DMA a promising candidate for improving the thermal stability and fire safety of lithium-ion electrolytes.

However, the relatively high viscosity of DMA[28,29] and its moderate polarity may negatively impact ionic transport, particularly at low temperatures. To mitigate these limitations, suitable co-solvents such as EC or propylene carbonate (PC) are incorporated. By deliberately avoiding linear carbonates and eliminating $LiPF_6$, this work aims to develop an electrolyte system with improved thermal stability and enhanced intrinsic safety while maintaining sufficient electrochemical performance.

The resulting DMA-based electrolytes are systematically evaluated with respect to ionic conductivity, electrochemical stability, flash point, thermal stability, and cycling performance over a wide temperature range. The optimized formulations are further characterized in terms of composition, viscosity, and density. In comparison with the reference electrolyte LP40 (1 M $LiPF_6$ in EC:DEC), the LiBOB–DMA systems exhibit a markedly increased flash point and significantly improved cycling stability at elevated temperatures, while retaining sufficient ionic conductivity and electrochemical stability for practical cell operation. These results highlight the potential of DMA-based electrolytes as safer alternatives to conventional carbonate-based systems for lithium-ion batteries.

2 Experimental

2.1 Materials

Dimethyl adipate (DMA, ≥99% purity, Fisher Scientific, Schwerte, Germany) and propylene carbonate (PC, ≥99.7% purity, Carl Roth, Karlsruhe, Germany) were transferred into an argon-filled glovebox with a residual moisture level below 0.5 ppm. Inside the glovebox, the solvents were further dehydrated overnight by the addition of a molecular sieve (pore size ≈ 0.3 nm). The molecular structure of DMA is shown in Fig. 1.

The solvent ethylene carbonate (EC, 99% purity, Sigma Aldrich, Taufkirchen, Germany) and the lithium salt lithium bis(oxalato)borate (LiBOB, Sigma Aldrich, Taufkirchen, Germany) were opened in the glovebox and used without further purification.

For reference measurements, the commercial electrolyte LP40 (1 M $LiPF_6$ in EC : DEC 1 : 1 wt, from E-Lyte Innovations, Kaiserslautern, Germany) was utilized.

The melting point, flash point, and boiling point of the solvents used in this study (DMA, EC, and PC) are listed in Table 1. For comparison, the corresponding values of DEC, which is present only in the reference electrolyte LP40, are also included.

Graphite electrodes with an areal capacity of 2.9 mAh cm^{-2} (supplied by Varta AG, Ellwangen, Germany) were punched into 16 mm diameter disks. Lithium nickel manganese cobalt oxide (NCM 622) electrodes with areal capacities of 1.3 mAh cm^{-2} (provided by Münster Electrochemical Energy Technology, Münster, Germany) and 2.9 mAh cm^{-2} (supplied by Varta AG, Ellwangen, Germany) were punched into 15 mm diameter disks. All electrodes were subsequently dried in a vacuum oven (B-585, Büchi Labortechnik AG, Flawil, Switzerland) at 120 °C for 16 h at a pressure below 50 mbar. Separators (type FS 2190, Freudenberg, Weinheim, Germany; thickness ≈ 200 μm) were punched into 19 mm disks and dried under the same conditions.

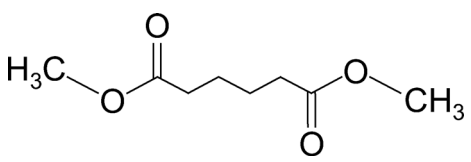

Fig. 1 Structural formula of dimethyl adipate (DMA).[30]

Table 1 Melting point (T_{MP}), flash point (T_{FP}) and boiling point (T_{BP}) of the used solvents DMA,[27,28] EC,[31–33] PC[31,32,34] and DEC[32,35]

	DMA	EC	PC	DEC
T_{MP} (°C)	8	36	−49	−43
T_{FP} (°C)	107	145	135	25
T_{BP} (°C)	227	248	242	126

2.2 Electrolyte preparation

All electrolytes were prepared inside a LABstar glovebox from M. Braun Inertgas-Systeme (Garching, Germany) under an argon atmosphere, where the water and oxygen levels were maintained below 0.5 ppm. First, the conducting salt was accurately weighed, followed by the addition of the solvents. The resulting mixture was then placed on a magnetic stirrer and continuously stirred until the salt was completely dissolved.

2.3 Cell assembly

Cell assembly was also carried out inside the glovebox. For electrochemical characterization, CR2032 housings were used, while CR2016 housings were employed for calorimetric measurements; both types were from PI-KEM Limited (Tamworth, Staffordshire, United Kingdom) and made of stainless steel 304. The cells were assembled by first placing the larger graphite electrode at the center of the lower housing part, followed by the separator. Subsequently, 70 μL of electrolyte were added, and the NCM electrode was placed on top. A spacer and spring were then positioned on the NCM electrode, and the cell was finally sealed using the digital pressure controlled electric crimping machine MSK-160E from MTI Corporation (Richmond, CA, USA).

2.4 Cell tests

To evaluate and optimize the performance of the cells with the new electrolyte, C-rate tests, aging experiments, and measurements at various temperatures were conducted. All electrochemical measurements were carried out using a CTS battery tester (BaSyTec, Asselfingen, Germany). During the entire testing procedure, the cells were maintained at the desired temperature inside an IPP 110 climate chamber (Memmert, Schwabach, Germany). Prior to the actual testing, all cells underwent formation consisting of three cycles at C/10, followed by three formation cycles at C/5 using constant current (CC) charge and CC discharge. The voltage window was set between 2.5 V (lower cut-off) and 4.2 V (upper cut-off). For each measurement, unless stated otherwise, at least two identical and fully functional cells were assembled and tested, and the reported values represent the mean of these cells.

2.5 Scanning electron microscope (SEM) measurements

Post-mortem analysis of the electrodes was conducted using a JSM-IT800 scanning electron microscope (JEOL, Tokyo, Japan). Top-view images were acquired using a secondary electron detector (SED) to investigate the surface morphology of the electrodes. All measurements were conducted in high-vacuum mode at an accelerating voltage of 3 kV and a working distance ranging from 8.9 to 10.7 mm.

Prior to SEM analysis, the cells were discharged to 2.5 V using a constant-current/constant-voltage (CCCV) protocol. Subsequently, the cells were disassembled inside an argon-filled glovebox. The electrodes were carefully removed, rinsed with dimethyl carbonate (DMC) to eliminate residual electrolyte, and left to dry for approximately 24 h inside the glovebox. After drying, the samples were transferred into a hermetically sealed transfer vessel and transported to the SEM without exposure to ambient air, thereby preventing atmospheric contamination and preserving the electrode surface state for analysis.

2.6 Linear sweep voltammetry (LSV) measurements

For linear sweep voltammetry (LSV) measurements, cells were assembled using lithium metal as both counter and reference electrode, while the working electrodes consisted of the active materials investigated in this study (graphite for reduction stability and NCM622 for oxidation stability), following previously reported cell configurations relevant for practical electrolyte stability evaluation.[36,37] The cells were assembled in ECC-Ref housings (EL-Cell, Hamburg, Germany). The electrochemical stability window of the electrolytes was evaluated using a Reference 3000 AE potentiostat (Gamry, Warminster, PA, USA). Measurements were initiated at the open-circuit voltage (OCV) and swept towards 6.0 V *vs.* Li/Li^+ for oxidative stability or down to 0.01 V *vs.* Li/Li^+ for reductive stability. A scan rate of 0.1 mV s^{-1} was applied throughout all measurements.

2.7 Electrolyte conductivity measurements

The ionic conductivity of the electrolytes was measured using a platinized HTCC conductivity cell (BioLogic, Seyssinet-Pariset, France) connected to a Reference 3000 AE from Gamry (Warminster, PA, USA). For temperature-dependent measurements, the conductivity cell was immersed in the water bath of a Proline RP 845 thermostat (Lauda, Lauda-Königshofen, Germany), and the resistance was recorded at 1000 Hz in 5 °C increments over the range of 5 to 60 °C. Ionic conductivity values were then calculated from the measured resistances using the cell constant, which had been previously determined with a standard electrical conductivity solution. The reported ionic conductivities represent the mean of two independently performed measurements.

2.8 Density measurements

Temperature-dependent density measurements were performed using a DMA 4500 M densitometer (Anton Paar, Graz, Austria). Approximately 1 mL of electrolyte was analyzed over the temperature range of 15 to 45 °C, with a temperature uncertainty $u(T)$ of 0.01 °C.

2.9 Viscosity measurements

The dynamic viscosity was measured using a rotational rheometer (Gemini HR Nano, Malvern, Worcestershire, UK) over a

temperature range of 15–45 °C in a cone–plate configuration (40/1°) with a gap of 30 μm. Measurements were conducted in a shear rate range of 50–180 s^{-1}. As no shear-rate dependence of the viscosity was observed, confirming Newtonian behavior, the reported values represent the average over this shear rate range. A solvent trap was used to minimize evaporation during the measurements. The dynamic viscosities were corrected based on reference measurements using a certified viscosity standard. The corrected values were obtained by applying a temperature-dependent correction factor derived from the ratio between certified and experimentally determined reference values.

2.10 Flash point measurement

The flash point of the electrolyte formulations was evaluated using an NPV Tech flash point tester (Normalab, Valliquerville, France). The instrument operates according to the rapid-equilibrium closed-cup procedure described in ISO 3679. It accommodates a temperature range from −30 to 300 °C and continuously records the ambient pressure *via* an integrated barometer, enabling automatic correction of the measured flash point to standard pressure. For measurements conducted below 100 °C, 2 mL of solvent were used, whereas 4 mL were required for tests at higher temperatures.

The determination procedure consisted of two stages, beginning with an automated scan to obtain an initial estimate of the flash point. In this mode, the filled test cup was heated at a predefined heating rate, and the ignition source was applied at each full degree increment. Detection of ignition terminated the automatic run and provided an approximate value.

Subsequently, the precise flash point was determined using manual measurements performed in accordance with ISO 3679. A fresh solvent sample was heated to a selected temperature and exposed to the ignition source to check for flammability. The first manual test was set 2 K below the ignition temperature identified during the automatic scan. If no ignition occurred, additional measurements were performed with freshly refilled samples, increasing the test temperature by 1 K in each step until a flash was observed. The temperature at which ignition first occurred was recorded as the flash point.

2.11 Gas chromatography (GC) measurements

Gas chromatography (GC) measurements were performed following a previously reported procedure.[38] Briefly, analyses were carried out on a Clarus 690 GC system (PerkinElmer) equipped with an autosampler, a flame ionization detector (FID), and a mass spectrometer (SQ 8T). A capillary column (Rxi-5Sil MS, 30 m × 0.25 mm × 0.25 μm) was used, and the gas flow was split post-separation to enable simultaneous MS and FID detection. Samples were injected in split mode (0.5 μL, 250 °C inlet temperature). The oven temperature was programmed from 40 °C to 320 °C at 20 °C min^{-1}. Helium was used as carrier gas, with hydrogen and air supplied for FID operation. MS detection was performed in scan mode (*m*/*z* 33–350). Data acquisition and analysis were conducted using Turbomass and TotalChrom software. Compounds and impurities were identified by comparison with reference substances and NIST database spectra.

2.12 Differential scanning calorimetry (DSC) measurements

Thermal properties of the electrolyte formulations were investigated using differential scanning calorimetry (DSC). High-temperature measurements were performed using a DSC 250 instrument (TA Instruments, New Castle, DE, USA) equipped with high-temperature, high-pressure stainless steel pans with a maximum volume of 35 μL, suitable for a temperature range from ambient to 550 °C. The hermetic pans are rated for pressures up to 200 bar at ≤380 °C, with reduced maximum pressure limits of 60 bar at 550 °C. Sample preparation was conducted in an argon-filled glovebox to prevent exposure to moisture and oxygen. Approximately 3 μL of electrolyte were transferred into the pans using a microliter pipette, and the exact sample mass was determined using an analytical balance. An empty pan, sealed under the same inert conditions, was used as reference. After sealing, the pans were removed from the glovebox and placed in the DSC instrument. The measurements were performed under a constant flow of high-purity nitrogen as purge gas. A linear heating program with a heating rate of 5 °C min^{-1} was applied from 35 to 400 °C.

Low-temperature DSC measurements were performed using a DSC 204 system (NETZSCH, Selb, Germany). Approximately 36 mg of electrolyte were sealed in aluminum crucibles inside an argon-filled glovebox. The measurement protocol consisted of two consecutive cooling and heating cycles, with only the second heating used for evaluation. Measurements were conducted under a constant flow of high-purity argon as purge gas, using a heating rate of 10 °C min^{-1} over a temperature range from −135 to 70 °C. Data evaluation followed Ding *et al.*[39] and Höhne *et al.*[40] The glass transition temperature (T_g) was determined from the inflection point, and the liquidus temperature (T_{liq}) from the peak of the endothermic transition. Detailed experimental procedures and a general description of the electrochemical curve interpretation are provided in ref. 41.

2.13 Thermal abuse test

Thermal abuse behavior was investigated using the heat–wait–seek (HWS) methodology in an ES ARC calorimeter (Thermal Hazard Technology, Bletchley, UK). This calorimeter provides the sensitivity necessary to monitor the thermal response of low-capacity coin cells with capacities around 5 mAh.[42,43] To obtain a measurable thermal signal, four individual cells were assembled into a stack for each experiment, resulting in a total capacity of approximately 9 mAh. The cells were secured together with heat-resistant tape (3M Industrial Business, Neuss, Germany), and the so-called bomb thermocouple type E was positioned at the center of the stack to accurately measure the sample temperature. The assembled stack was placed centrally inside the calorimeter to ensure uniform heating. Prior to testing, the ARC system was calibrated using coin-cell dummies with comparable thermal mass under identical experimental conditions, followed by a drift test to ensure instrument stability.

The HWS procedure consists of a sequence of heating, equilibration, and self-heating detection steps. Initially, the sample is heated from ambient temperature to 35 °C, after which subsequent heating steps increase the temperature by 5 K. Each heating step is followed by a waiting period of 20 min to allow the cell stack to reach thermal equilibrium. During the subsequent seek phase, temperatures recorded by two thermocouples—one near the internal heater and the bomb thermocouple at the sample—are continuously compared. The temperature change of the sample during the seeking phase is used to determine the heating rate. When the rate exceeds the threshold of 0.02 °C min^{-1}, the system identifies the onset of self-heating and switches to an (approximately) adiabatic mode that minimizes heat losses to the surroundings because the heaters in the calorimeter chamber follow the increase in cell temperature. In this mode, exothermic reactions dominate the temperature evolution until either thermal runaway is triggered or the energy released by reactive processes is depleted. In the latter case, the next 5 K heating step follows.

Events such as gas venting or intermediate endothermic reactions can temporarily suppress self-heating, in which case the calorimeter resumes stepwise heating until exothermic activity reappears or runaway conditions develop. A detailed description of this methodology is provided in ref. 44. For safety reasons, experiments were terminated at 300 °C. For each electrolyte, the measurements were performed in triplicate, and the presented data correspond to a representative measurement.

3 Results and discussion

In this study, DMA is investigated as a non-fluorinated and potentially less hazardous electrolyte solvent for lithium-ion batteries. Due to its favorable physical properties, and in combination with the conducting salt LiBOB, DMA offers the potential to enhance both the thermal stability and the intrinsic safety of the electrolyte. The overarching goal of this work is to formulate an electrolyte with enhanced thermal robustness by avoiding linear carbonates and eliminating $LiPF_6$, while maintaining competitive electrochemical performance. The following section presents the electrochemical and thermal characterization of the resulting electrolyte systems, including a comparison with the standard electrolyte LP40.

3.1 Optimization of the LiBOB concentration and solvent composition

LiBOB is known to exhibit lower solubility than $LiPF_6$ in many common electrolyte solvents, which typically limits its use to lower salt concentrations. As a first step, the ionic conductivity of LiBOB was therefore evaluated in a solvent mixture consisting of 85% DMA and 15% EC for several salt concentrations, as listed in Table 2. At 25 °C, the conductivity reaches a maximum at salt concentrations of 0.6 and 0.7 m (mol kg^{-1}). At 10 °C, the conductivity is slightly higher for 0.6 m, whereas at 40 °C, the 0.7 m electrolyte exhibits the higher conductivity.

Table 2 Ionic conductivity κ of LiBOB at various concentrations m in 85% DMA and 15% EC at different temperatures

m (mol kg^{-1})	$\kappa_{10\,°C}$ (mS cm^{-1})	$\kappa_{25\,°C}$ (mS cm^{-1})	$\kappa_{40\,°C}$ (mS cm^{-1})
0.5	n.m.	2.05	n.m.
0.6	1.27	2.13	3.04
0.7	1.25	2.13	3.12
0.8	n.m.	2.07	n.m.

n.m. = not measured.

Subsequently, C-rate tests ranging from C/10 to 2C were performed using the 0.6, 0.7, and 0.8 m electrolytes to evaluate their electrochemical behavior in practical cells. The corresponding results are presented in Fig. 2. Among the tested concentrations, the 0.7 m electrolyte delivered the highest extractable capacity. Therefore, a concentration of 0.7 m was selected for further optimization of the solvent composition in order to improve both ionic conductivity and overall cell performance.

Using the previously identified concentration of 0.7 m LiBOB, the ionic conductivity at 25 °C was subsequently measured for various solvent mixtures. All formulations were based on a minimum DMA content of 60 wt%, complemented by different weight fractions of EC and PC. The results of these conductivity measurements are summarized in Table 3.

The data show that the addition of EC or PC leads to an increase in ionic conductivity, with both co-solvents exhibiting a comparable effect on conductivity enhancement.

Based on these results, three electrolyte formulations were selected for further characterization in order to evaluate their performance in full cells: 0.7 m LiBOB in DMA : EC (60 : 40 wt), 0.7 m LiBOB in DMA : PC (60 : 40 wt), and 0.7 m LiBOB in DMA : EC : PC (60 : 20 : 20 wt). These compositions were subjected to additional electrochemical testing to assess their suitability as improved electrolyte systems.

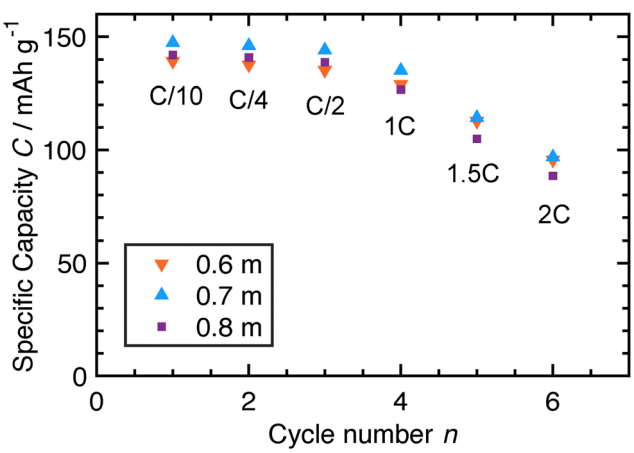

Fig. 2 Specific discharge capacity at various C-rates for NCM/graphite cells using a solvent composition of 85% DMA and 15% EC (by weight) with different LiBOB concentrations. The C-rate performance represents the mean of two independently tested cells for each configuration.

Table 3 Investigated solvent mixtures by weight (wt) combined with 0.7 m LiBOB and their ionic conductivity at 25 °C

DMA	EC	PC	$\kappa_{25\,°C}$ (mS cm^{-1})
100%	—	—	1.42
85%	15%	—	2.13
60%	40%	—	2.77
60%	—	40%	2.76
60%	20%	20%	2.76

3.2 Life cycle performance at different temperatures

The aging behavior of cells with the different electrolytes was evaluated through cycling tests conducted over at least 100 cycles at various temperatures. Following the formation procedure described in the experimental section, cells not otherwise specified had a theoretical capacity of approximately 2.3 mAh and were charged using a constant-current/constant-voltage (CCCV) protocol at C/2 (cut-off current: C/10) and discharged at C/2 under constant-current (CC) conditions.

3.2.1 Ambient temperature (25 °C). Fig. 3 presents the cycling performance of the LiBOB–DMA-based electrolytes in comparison with the standard electrolyte LP40 at 25 °C. Cells containing LiBOB–DMA-based electrolytes exhibit a lower usable capacity at the beginning of cycling compared to LP40. This reduced initial capacity points to increased overpotentials within the cells, which can be attributed to the lower ionic conductivity of the LiBOB–DMA-based electrolyte formulations. Nevertheless, it is also evident that cells containing the LiBOB–DMA-based electrolytes exhibit significantly lower degradation over cycling. After 100 cycles, all LiBOB–DMA-based formulations retain more than 99% of the discharge capacity measured in the first cycle after formation. In contrast, cells with the reference electrolyte LP40 show a markedly stronger capacity fade, reaching only 94% after 100 cycles.

When comparing the three electrolytes based on LiBOB and DMA in Fig. 3(a), their overall behavior is very similar. However, the highest discharge capacity is obtained with the DMA–EC electrolyte, followed by the DMA–PC formulation. The DMA–EC–PC electrolyte shows the lowest accessible capacity among the three systems.

To further investigate the long-term performance, additional cycling tests were conducted with larger 5 mAh cells. In these experiments, only the DMA–EC electrolyte and the reference LP40 electrolyte were evaluated. The cells were charged using a C/4 CCCV protocol and discharged at C/4 under CC conditions. The results, shown in Fig. 3(b), demonstrate that after 1000 cycles, the LiBOB–DMA cell still retains over 80% of its initial post-formation capacity, whereas the LP40 cell retains only approximately 50%.

3.2.2 Elevated temperatures (40 °C and 60 °C). Furthermore, cycling tests at higher temperatures were conducted to assess the thermal stability of the electrolytes. The results obtained at 40 °C are presented in Fig. 4(a). At the beginning of cycling, the LiBOB–DMA-based electrolytes and the reference electrolyte LP40 exhibit comparable usable capacities. However, the capacity fade of the LP40 cells is significantly more

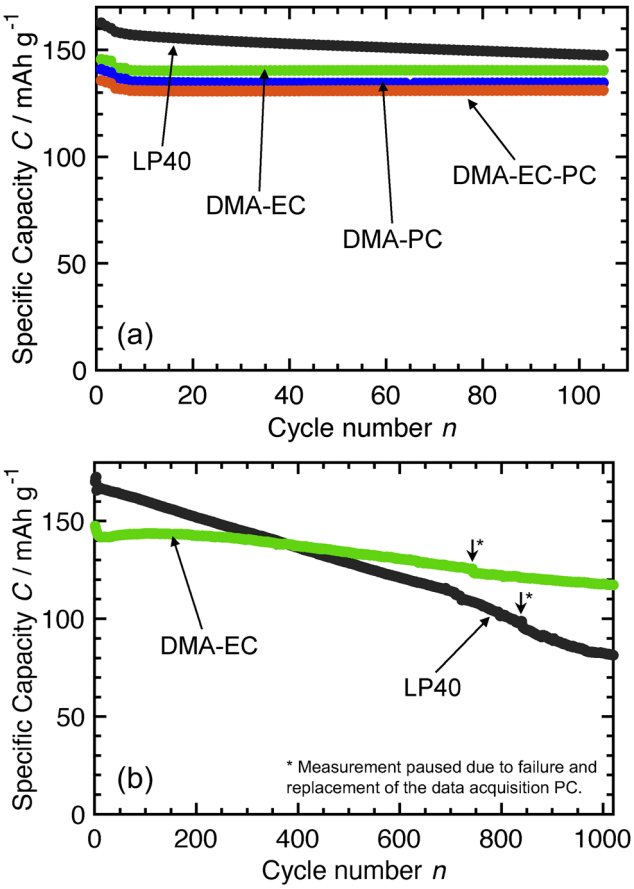

Fig. 3 Specific discharge capacity of NCM/graphite cells containing 0.7 m LiBOB in DMA:EC, 0.7 m LiBOB in DMA:PC, 0.7 m LiBOB in DMA:EC:PC and the standard electrolyte LP40 at T_1 = 25 °C. The first three cycles are formation cycles at C/10, followed by three formation cycles at C/5. After formation, the cells were charged using (a) a C/2 CCCV protocol and discharged at a C/2 CC rate (cell capacity: 2.3 mAh) and (b) a C/4 CCCV protocol and discharged at a C/4 CC rate (cell capacity: 5 mAh). In (a), the data represent the mean of two independently tested cells per configuration. In (b), the data are based on a single cell per configuration due to the extended measurement time and the limited number of available test channels. Cells using the LiBOB–DMA-based electrolytes exhibit substantially lower capacity fade compared to cells with the LP40 electrolyte.

pronounced than that of the LiBOB–DMA-based cells. After 240 cycles, the LiBOB–DMA-based electrolytes retain at least 95% of the capacity measured in the first post-formation cycle, whereas the LP40 cells maintain only about 72% under identical cycling conditions.

The corresponding performance at 60 °C is shown in Fig. 4(b). Here, the same trend becomes even more pronounced. The usable capacity of the LP40 cell drops sharply within the first few cycles, and the progression changes from an approximately linear decay, as observed at lower temperatures, to a distinctly exponential decline. After 240 cycles, only 39% of the initial post-formation capacity remains. It should be noted that the LP40 cell already exhibits a significantly lower capacity at the start of cycling compared to the LiBOB–DMA-based cells. This pronounced degradation is mainly attributed to the thermal decomposition of the conducting salt $LiPF_6$, which is

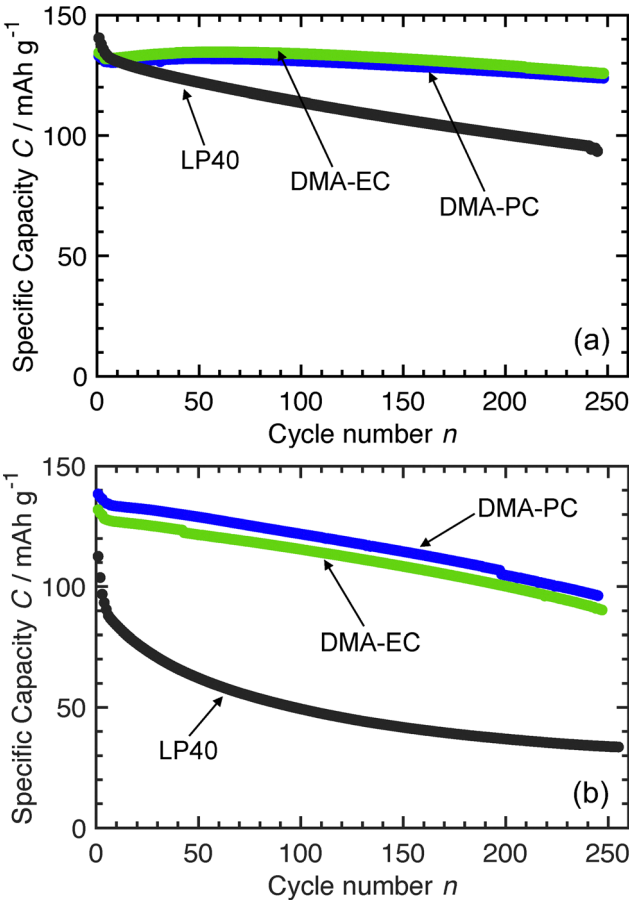

Fig. 4 Specific discharge capacity of NCM/graphite cells containing 0.7 m LiBOB in DMA:EC, 0.7 m LiBOB in DMA:PC and the standard electrolyte LP40 at (a) T_2 = 40 °C and (b) T_3 = 60 °C. The first three cycles are formation cycles at C/10, followed by three formation cycles at C/5. After formation, the cells were charged using a C/2 CCCV protocol and discharged at a C/2 CC rate. In (a), the data represent the mean of two independently tested cells per configuration. In (b), the data are based on a single cell per configuration due to a limited number of available test channels. Cells with LiBOB–DMA-based electrolytes exhibit substantially higher stability at elevated temperatures compared to those containing LP40.

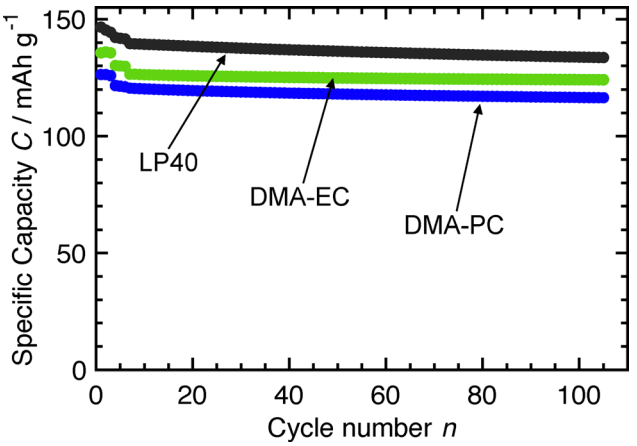

Fig. 5 Specific discharge capacity of NCM/graphite cells containing 0.7 m LiBOB in DMA:EC, 0.7 m LiBOB in DMA:PC and the standard electrolyte LP40 at T_4 = 10 °C. The first three cycles are formation cycles at C/10, followed by three formation cycles at C/5. After formation, the cells were charged using a C/2 CCCV protocol and discharged at a C/2 CC rate. The data represent the mean of two independently tested cells per configuration. Cells with LiBOB–DMA-based electrolytes exhibit a slightly lower capacity loss compared to cells with the LP40 electrolyte.

strongly accelerated at elevated temperatures. In contrast, the cells containing the LiBOB–DMA-based electrolytes continue to exhibit an almost linear capacity fade, even at 60 °C. After 240 cycles, these cells still retain 71% of their initial capacity, demonstrationg the significantly improved thermal stability of the LiBOB–DMA systems at high operating temperatures.

3.2.3 Low temperature (10 °C). Finally, the cycling performance at 10 °C was investigated, and the results are shown in Fig. 5. The absolute usable capacity of the LiBOB–DMA cells is lower than that of the LP40 cells at this temperature, in contrast to the behavior observed at higher temperatures. This reduction is primarily due to the lower ionic conductivity of the LiBOB–DMA-based electrolytes at low temperatures. Nevertheless, the LiBOB–DMA cells still exhibit slightly better capacity retention over the first 100 cycles compared to the LP40 cell, although the differences are considerably smaller than at elevated temperatures. After 100 cycles, the LiBOB–DMA cells retain at least 97% of their initial capacity, whereas the LP40 cells retain 96%.

3.2.4. Overall temperature-dependent cycling stability. The cycling results at different temperatures consistently demonstrate that the new LiBOB–DMA-based electrolyte provides enhanced stability and reduced degradation compared to the standard LP40 electrolyte. This effect becomes more pronounced at elevated temperatures, making the new electrolytes clearly superior to conventional standard electrolytes already at operating temperatures of 40 °C. The enhanced stability not only helps to maintain the usable capacity but is also expected to improve the long-term cycle life of the cells. Notably, even at 25 °C, the capacity retention curves of the LiBOB–DMA-based electrolyte and LP40 intersect at approximately 400 cycles, after which the DMA-based system exhibits a consistently higher remaining capacity, indicating a long-term stability advantage also under moderate operating conditions. This improved performance can be attributed to the absence of $LiPF_6$, which begins to decompose already at temperatures around 55 °C[45] or even lower.[46] In contrast, LiBOB exhibits significantly higher thermal stability and decomposes at temperatures exceeding 300 °C,[47] thereby effectively suppressing salt-driven degradation reactions within the investigated temperature range.

3.3 Voltage profiles at different temperatures

The stability of the electrolytes is also reflected in the voltage profiles at different temperatures, as shown in Fig. 6. Both the voltage behavior and the extractable capacity of the cells change only slightly over the considered temperature range of 20 to 60 °C. Only at 10 °C is a noticeable drop in voltage and capacity observed, which can be attributed to the lower ionic conductivity of the electrolyte at low temperatures. In the figure, a

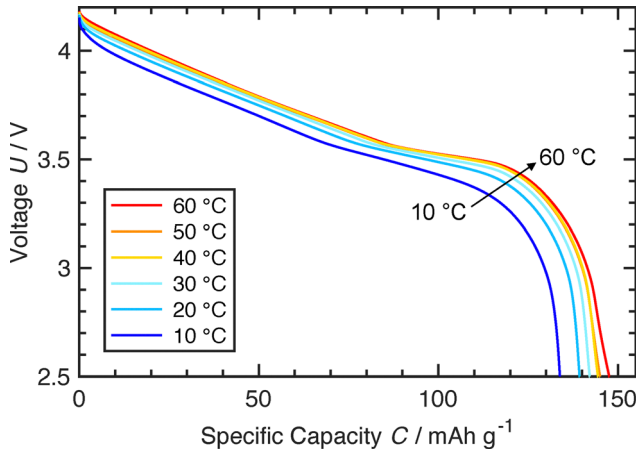

Fig. 6 Voltage profiles of a NCM/graphite cell with 0.7 m LiBOB in DMA : EC (60 : 40 wt) at different temperatures and a C-rate of C/4. The maximum extractable capacity is observed at 60 °C. Even at 10 °C, a large fraction of this capacity remains accessible. The experiment was performed three times independently, and the data shown represent a representative measurement.

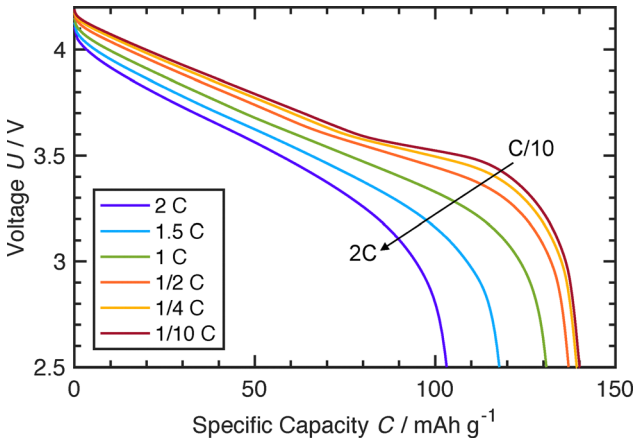

Fig. 7 Voltage profiles and specific discharge capacity of a NCM/graphite cell with 0.7 m LiBOB in DMA : EC (60 : 40 wt) electrolyte at T = 25 °C, recorded at C-rates of C/10, C/4, C/2, 1C, 1.5C and 2C. Up to a C-rate of 1C, more than 90% of the discharge capacity remains accessible, whereas at higher C-rates a pronounced reduction in transferable charge is observed. The experiment was performed three times independently, and the data shown represent a representative measurement.

representative measurement is shown. A total of three independent measurements were performed, and Table 4 summarizes the corresponding mean values and standard deviations.

3.4 C-rate performance of LiBOB–DMA-based cells

The rate capability of the LiBOB–DMA-based electrolyte was evaluated by cycling NCM/graphite cells at various discharge C-rates at 25 °C, as shown in Fig. 7. The cells were discharged at different C-rates of C/10, C/4, C/2, 1C, 1.5C and 2C, while after each discharge they were recharged under identical conditions using a C/6 constant-current step followed by a constant-voltage phase. This procedure ensured that each subsequent discharge started from a comparable and well-defined state of charge.

The experiment was performed three times independently. The data shown in Fig. 7 represent a representative measurement, while the corresponding mean values and standard deviations of the three independent cells are summarized in Table 5.

The results indicate stable electrochemical performance at moderate discharge rates, with more than 90% of the capacity remaining accessible up to a discharge rate of 1C, compared to the capacity at C/10. At higher C-rates, the extractable capacity decreases significantly, which can be attributed to increased polarization and kinetic limitations under elevated current densities.

Table 4 Values represent mean ± standard deviation of the specific capacity of three independently tested NCM/graphite cells with 0.7 m LiBOB in DMA : EC (60 : 40 wt) at different temperatures and a C-rate of C/4

Temperature/°C	Specific capacity/mAh g^{-1}
10	131 ± 3
20	135 ± 3
30	138 ± 4
40	140 ± 4
50	141 ± 3
60	144 ± 4

Table 5 Values represent mean ± standard deviation of the specific capacity of three independently tested NCM/graphite cells with 0.7 m LiBOB in DMA : EC (60 : 40 wt) at different C-rates at T = 25 °C

C-rate	Specific capacity/mAh g^{-1}
C/10	137 ± 3
C/4	136 ± 3
C/2	134 ± 3
1C	126 ± 6
1.5C	113 ± 7
2C	99 ± 7

3.5 Post-mortem SEM analysis

Fig. 8 and 9 show SEM images of the investigated electrodes, providing an overview of the electrode morphology and local surface features. Samples (a/d) correspond to pristine electrodes, (b/e) represent electrodes from a cell with 0.7 m LiBOB in DMA:EC electrolyte after formation, and (c/f) show electrodes from a cell with 0.7 m LiBOB in DMA:EC electrolyte after 1000 cycles at 25 °C (cell shown in Fig. 3(b)). The macroscopic photograph of the graphite electrode after 1000 cycles shown in Fig. 9, reveals a heterogeneous surface appearance, with some regions showing a light gray discoloration, while other regions retain the characteristic black color of graphite. Therefore, SEM images were acquired from two distinct regions of interest, which are marked on the electrode surface.

The pristine NCM electrode (Fig. 8(a)) consists of homogeneous spherical secondary particles with smooth surfaces and no visible defects. After formation (Fig. 8(b)), minor changes are observed, while the overall morphology remains essentially

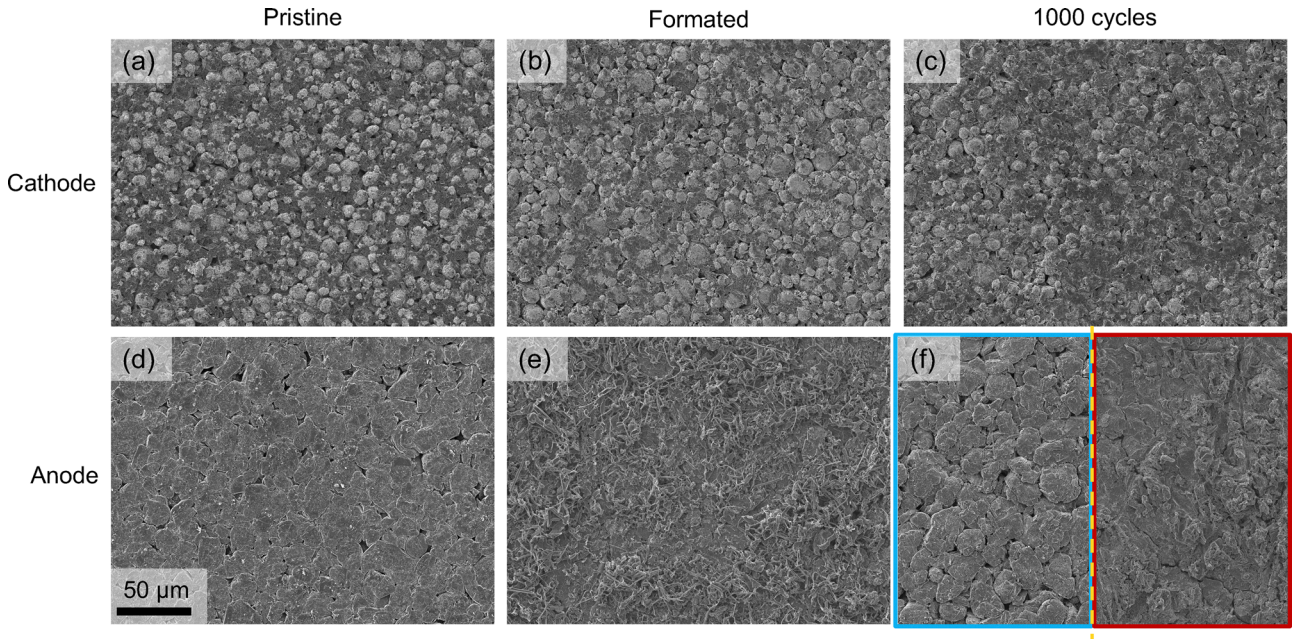

Fig. 8 SEM images of NCM and graphite electrodes. (a)–(c) NCM electrode and (d)–(f) graphite electrode. (a/d) Pristine electrodes, (b/e) after formation in 0.7 m LiBOB in DMA:EC electrolyte, and (c/f) after 1000 cycles at 25 °C in 0.7 m LiBOB in DMA:EC electrolyte.

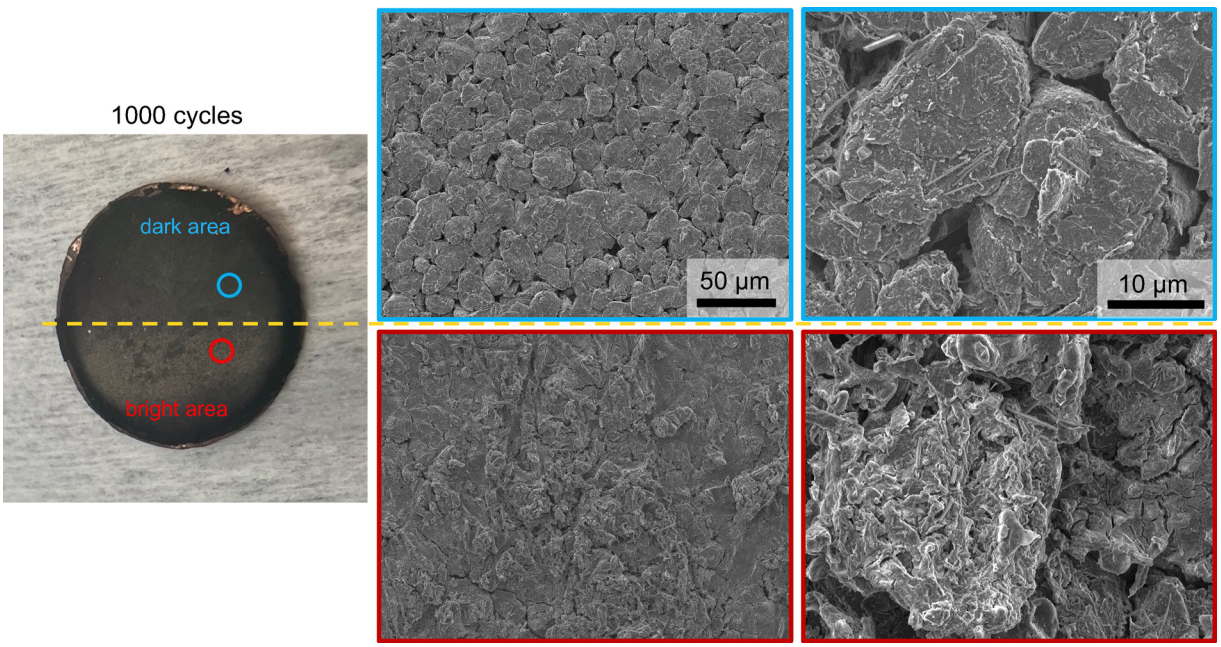

Fig. 9 Images of the graphite electrode after 1000 cycles at 25 °C in 0.7 m LiBOB in DMA:EC electrolyte. The macroscopic image of the cycled graphite electrode shows non-uniform surface appearance. Dark (top) and bright (bottom) regions were selected for SEM analysis at different magnifications.

unchanged, without clear structural differences compared to the pristine state. After 1000 cycles (Fig. 8(c)), the NCM electrode shows only subtle ageing effects, and the overall particle morphology is largely preserved, with no pronounced structural degradation evident.

The pristine graphite electrode (Fig. 8(d)) shows well-defined graphite flakes with clean and homogeneous surfaces. After formation (Fig. 8(e)), a distinct surface layer covering the graphite particles is visible, while the underlying graphite structure remains observable in the background. After 1000 cycles, the graphite electrode shows clear spatial heterogeneity. The dark region (Fig. 9(top)) retains clearly distinguishable graphite flakes with only limited surface coverage. Compared to the pristine electrode, however, the surface appears rougher

and more porous. In contrast, the bright region (Fig. 9(bottom)) shows a pronounced surface layer covering the graphite flakes, resulting in a strongly modified surface appearance. The morphology is consistent with commonly reported ageing phenomena in graphite electrodes, showing a dense surface layer with almost no visible pores, indicative of SEI thickening. In addition, pronounced through-going cracks are observed across the field of view, distinct from pre-existing interparticle gaps, suggesting mechanically induced degradation. Thus, the contrast between the two macroscopically distinct regions of the graphite electrode after 1000 cycles is also reflected in the corresponding SEM images, indicating locally varying ageing behaviour that persists from the macroscopic to the microscopic scale.

3.6 Flash point and conductivity

One of the primary motivations behind the development of the new electrolyte formulation is the substantial improvement of its intrinsic fire safety. Conventional carbonate-based electrolytes such as LP40 exhibit a relatively low flash point of approximately $T_{FP} \approx 37$ °C, which represents a significant safety concern, particularly under abusive or high-temperature operating conditions. In practical battery operation, cell temperatures can readily exceed 50 °C,[10] and in the presence of mechanical damage or internal short circuits this can promote the formation and ignition of flammable vapors.

In contrast, the newly developed DMA-based solvent systems DMA : EC (60 : 40 wt) and DMA : PC (60 : 40 wt) exhibit substantially higher flash points than the conventional reference electrolyte. Measurements performed according to ISO 3679 yield flash points of $T_{FP,DMA:EC} = 135 \pm 2$ °C for the DMA:EC mixture and $T_{FP,DMA:PC} = 123 \pm 2$ °C for the DMA:PC mixture. Relative to LP40 $T_{FP,LP40} = 37 \pm 2$ °C, this represents an increase of 98 K and 86 K, respectively.

These significantly elevated flash points demonstrate the enhanced intrinsic safety of the DMA-based solvent systems and indicate a considerably reduced flammability risk under practical battery operating conditions. This is particularly important given that the maximum working temperatures of lithium-ion cells are typically around 60 °C. Under these conditions, the DMA-based electrolytes remain far below their ignition thresholds, thereby providing a substantially enlarged safety margin compared to conventional carbonate-based systems. As a result, the risk of electrolyte ignition and the onset of thermal runaway is significantly reduced, especially under abusive or failure conditions such as overheating or mechanical damage.

Fig. 10 summarizes the temperature-dependent ionic conductivity of the two DMA-based electrolytes in comparison with the reference electrolyte LP40. Over the entire investigated temperature range from 5 °C to 60 °C, the conductivities of 0.7 m LiBOB in DMA : EC (60 : 40 wt) and 0.7 m LiBOB in DMA : PC (60 : 40 wt) are nearly identical, indicating that EC and PC exert a very similar influence on ion transport in the DMA-based solvent system. At $T = 25$ °C, the ionic conductivity amounts to 2.7 mS cm^{-1} for the DMA–EC and DMA–PC

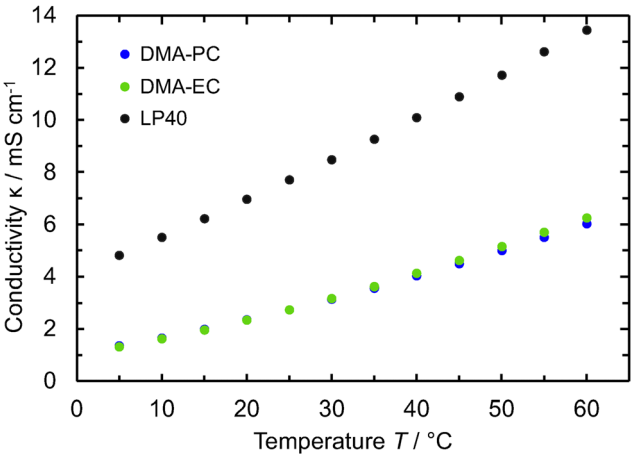

Fig. 10 Ionic conductivity of 0.7 m LiBOB in DMA : EC (60 : 40 wt), 0.7 m LiBOB in DMA : PC (60 : 40 wt), and the reference electrolyte LP40 in the temperature range from 5 °C to 60 °C. The conductivities of the DMA-based electrolytes are approximately two to three times lower than that of LP40, but remain within the same order of magnitude. Values represent the mean of two independently performed measurements.

electrolytes, respectively, whereas the reference electrolyte LP40 exhibits significantly higher values of 7.7 mS cm^{-1} under the same conditions.

Although the conductivities of the DMA-based electrolytes are approximately two to three times lower than that of LP40, they remain within the same order of magnitude across the entire temperature window. This suggests that the reduced conductivity does not originate from a fundamentally different transport mechanism, but rather from the higher viscosity and the distinct solvation environment of the DMA-based solvent mixtures, combined with the use of a different conducting salt, LiBOB instead of $LiPF_6$, which is known to exhibit lower ionic dissociation and mobility in solution.

3.7 Physicochemical properties and electrolyte composition

To further characterize the electrolyte systems, relevant physicochemical properties of the most promising formulations were examined in more detail. In the following, the DMA–EC (60 : 40 wt) electrolyte with 0.7 m LiBOB is compared to the reference electrolyte LP40, as both systems showed representative electrochemical behavior in the previous sections. Table 6 summarizes the temperature-dependent density, viscosity, and ionic conductivity of both electrolytes between 15 and 45 °C. The density of the DMA-based electrolyte is slightly lower than that of LP40 across the entire temperature range, while both systems show the expected linear decrease with increasing temperature.

The viscosity of the LiBOB–DMA–EC electrolyte is considerably higher than that of LP40, roughly by a factor of two over the full temperature range. This higher viscosity is in line with the lower ionic conductivity of the DMA-based system and contributes to the increased overpotentials and reduced rate capability at ambient and lower temperatures. Although the ionic conductivity of the DMA-based electrolyte is consistently lower

Table 6 Temperature-dependent density (ρ), viscosity (η), and ionic conductivity (κ) of LP40 and 0.7 m LiBOB in DMA:EC (60 : 40 wt). The DMA-based electrolyte is marked as DMA*. Uncertainties: density ± 0.0005 g cm^{-3}, viscosity ± 0.2 mPa s, conductivity ± 0.02 mS cm^{-1}

	ρ/g cm^{-3}		η/mPa s		κ/mS cm^{-1}	
T/°C	LP40	DMA*	LP40	DMA*	LP40	DMA*
15	1.236	1.227	5.4	13.6	6.22	1.96
25	1.225	1.217	4.4	9.6	7.71	2.77
35	1.214	1.207	3.5	6.8	9.25	3.62
45	1.205	1.197	3.1	5.3	10.89	4.61

than that of LP40, the values remain within the same order of magnitude. This suggests that, despite reduced ion mobility due to higher viscosity and differences in solvation, ionic transport is still sufficient for practical cell operation.

Additional gas chromatography (GC) measurements were performed to assess the composition and possible decomposition products of the electrolytes. Fig. 11 shows representative chromatograms of dichloromethane (DCM), LP40, and the LiBOB–DMA–EC system. The peak at 5.4 min corresponds to $CHCl_3$ as the main impurity in the solvent CH_2Cl_2. DEC (7.5 min) and EC (10.5 min) (LP40) as well as EC and DMA (15.0 min, DMA-based electrolyte) can clearly be observed in the electrolytes. In LP40, minor early-eluting peaks can be attributed to decomposition products such as POF_3, indicating initial $LiPF_6$ degradation. In contrast, no comparable peaks are observed for the DMA-based electrolyte, suggesting improved chemical stability under the investigated conditions. Since the samples were filtered through DCM prior to analysis to precipitate the poorly soluble conducting salt, non-volatile and sparingly soluble species are not detected. Under the applied conditions, impurities can typically be detected down to concentrations in the range of a few hundred ppm.

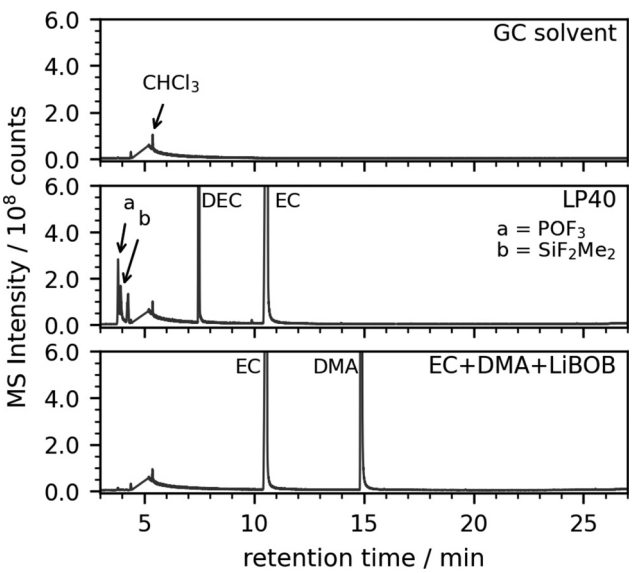

Fig. 11 Gas chromatograms of DCM (top), LP40 (middle), and the 0.7 m LiBOB in DMA : EC (60 : 40 wt) electrolyte (bottom). The main peaks are assigned to $CHCl_3$ (reference), DEC and EC (LP40), and EC and DMA (DMA-based electrolyte). Minor early-eluting peaks in LP40 (marked a and b) are tentatively assigned to decomposition products, including POF_3 and silicon-containing species. Additional minor peaks could not be unambiguously assigned.

3.8 Linear sweep voltammetry

The electrochemical stability of the DMA-based electrolyte was further evaluated by linear sweep voltammetry (LSV) and compared to the reference electrolyte LP40. Lithium metal was used as both counter and reference electrode. The measurements were initiated at the open-circuit voltage (OCV). For oxidation stability, NCM622 was employed as the working electrode and the potential was swept anodically up to 6.0 V *vs.* Li/Li$^+$ (Fig. 12(a)).

In the anodic scans, both electrolytes show an increase in current starting at approximately 3.6 V *vs.* Li/Li$^+$, which is attributed to the delithiation of the NCM622 electrode. Since no universally defined cut-off current density exists for determining the oxidative stability limit, a value of 0.5 mA cm^{-2} (at a scan rate of 0.1 mV s^{-1}) was selected based on previously

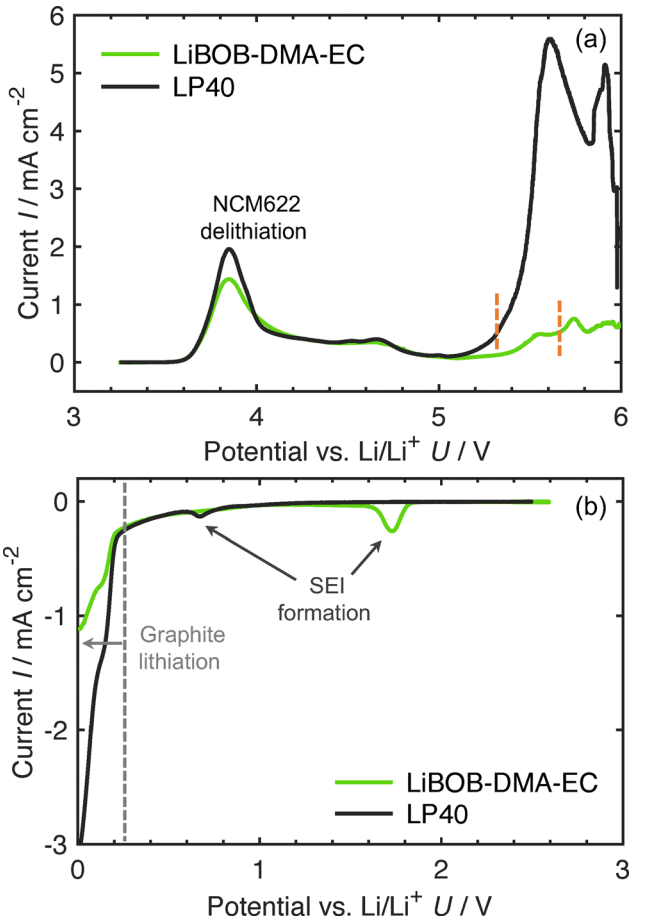

Fig. 12 Linear sweep voltammetry of 0.7 m LiBOB in DMA : EC (60 : 40 wt) and the reference electrolyte LP40, measured at a scan rate of 0.1 mV s^{-1} using lithium metal as both counter and reference electrodes. (a) Oxidation stability determined with NCM622 as the working electrode. The oxidative stability limits of the electrolytes, defined at a current density of 0.5 mA cm^{-2}, are indicated by dashed lines. (b) Reduction stability determined with graphite as the working electrode.

reported criteria.[36] Using this threshold, the oxidative stability limits are determined to be approximately 5.35 V for LP40 and 5.65 V for the DMA-based electrolyte. The oxidative stability limit determined for LP40 is consistent with previously reported values for carbonate-based $LiPF_6$ electrolytes on cathode working electrodes, which typically lie in the range of 5.2–5.5 V *vs.* Li/Li^+.[42] Independent of the selected current criterion, the earlier and more pronounced current increase observed for LP40 indicates a higher susceptibility to oxidative electrolyte decomposition compared to the DMA-based electrolyte. These results suggest an improved oxidative stability of the DMA-based electrolyte, reflected by the delayed onset of anodic current increase and the higher apparent oxidation stability limit compared to LP40.

For reduction stability, graphite was used as the working electrode and the potential was swept cathodically down to 0.01 V *vs.* Li/Li^+ (Fig. 12(b)). The cathodic LSV profiles exhibit distinct reduction features for the two electrolytes. For the LiBOB-based electrolyte, a pronounced increase in reduction current is observed at approximately 1.8–1.6 V *vs.* Li/Li^+, which is consistent with the reported reduction of LiBOB and the onset of LiBOB-derived interphase formation on graphite.[48] In contrast, the corresponding reduction feature for LP40 appears at lower potentials of approximately 0.8–0.6 V *vs.* Li/Li^+, in agreement with the reduction of carbonate solvents typically associated with SEI formation in $LiPF_6$-based electrolytes.[48] At potentials below approximately 0.25 V *vs.* Li/Li^+, both electrolytes show the characteristic current increase associated with graphite lithiation.

3.9 Differential scanning calorimetry

The thermal behavior of the electrolyte 0.7 m LiBOB in DMA : EC (60 : 40 wt) and the conventional reference electrolyte LP40 is shown in Fig. 13. Owing to instrumental limitations, the complete temperature range could not be covered in a single DSC measurement. Therefore, separate DSC experiments were performed for the high-temperature range (35 to 400 °C, Fig. 13(a)) and the low-temperature range (−135 to 70 °C, Fig. 13(b)). The heat flow signal (endothermic direction upward) is plotted as a function of temperature.

Fig. 13(a) shows the DSC thermograms obtained in the high-temperature range. The sample masses were highly comparable, with 4.4 mg for LP40 and 4.6 mg for the DMA-based electrolyte, ensuring a consistent basis for comparison. The thermogram of LP40 reveals the onset of thermal events at comparatively low temperatures. An initial endothermic transition is observed with a maximum at 224 °C, which is subsequently followed by a pronounced exothermic decomposition process peaking at 253 °C. This sequence indicates limited thermal stability and the occurrence of early-stage decomposition reactions in the conventional electrolyte system. In comparison, the DMA-based electrolyte exhibits a markedly delayed onset of thermal activity. The first detectable endothermic process appears at significantly higher temperature, with a peak at 308 °C, consistent with literature reports on the endothermic decomposition of LiBOB.[49] At higher

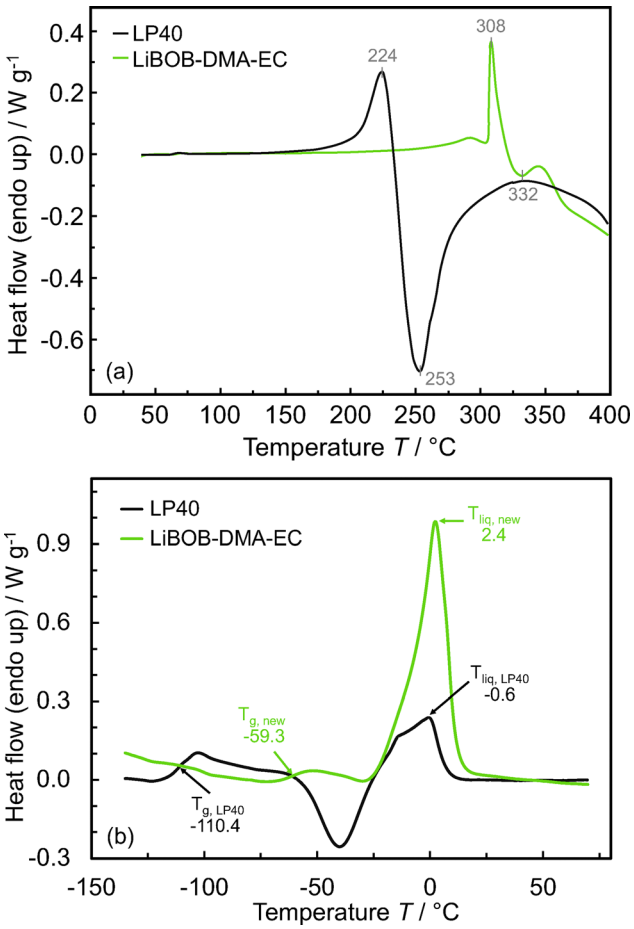

Fig. 13 Differential scanning calorimetry (DSC) curves of the 0.7 m LiBOB in DMA : EC (60 : 40 wt) electrolyte and the reference electrolyte LP40. The heat flow signal (endothermic up) is plotted as a function of temperature. (a) High-temperature range; samples were measured under comparable mass conditions (DMA-based electrolyte: 4.6 mg; LP40: 4.4 mg) at a heating rate of 5 °C min^{-1}. (b) Low-temperature range; samples were measured under comparable mass conditions (DMA-based electrolyte: 36.33 mg; LP40: 36.7 mg) at a heating rate of 10 °C min^{-1}.

temperatures, a subsequent exothermic event is observed, characterized by a small peak at 332 °C. The pronounced shift of both endothermic and exothermic features toward higher temperatures demonstrates an improved thermal stability of the DMA-based electrolyte relative to LP40. In particular, the delayed onset of exothermic decomposition is of relevance for thermal stability, as such exothermic processes are directly associated with heat release and can therefore be considered critical indicators for the thermal safety window of the electrolyte system.

Fig. 13(b) presents the DSC thermograms recorded in the low-temperature range. For LP40, the glass transition temperature (T_g) is determined to be −110.4 °C, while the liquidus temperature (T_{liq}) is observed at −0.6 °C. In contrast, the DMA-based electrolyte exhibits a significantly higher glass transition temperature of −59.3 °C, whereas the liquidus temperature remains comparable at 2.4 °C. The pronounced increase in T_g for the LiBOB-containing DMA electrolyte indicates reduced molecular mobility and stronger intermolecular interactions

compared to LP40. This behavior may be attributed to differences in ion–solvent interactions and solvent composition between the two electrolyte systems. Consequently, the DMA-based electrolyte is expected to exhibit reduced ionic transport at low temperatures, which is consistent with the lower conductivity observed in conductivity measurements. Despite the higher T_g, both electrolytes exhibit similar T_{liq} values and remain liquid near room temperature, indicating that the DMA-based formulation retains practical applicability despite its less favorable low-temperature characteristics.

3.10 Thermal abuse test

The thermal safety of the newly developed electrolyte system was evaluated using heat–wait–seek (HWS) experiments carried out in an accelerating rate calorimeter. Coin cells based on an NCM/graphite configuration were prepared using the newly developed electrolyte consisting of 0.7 m LiBOB in DMA : EC (60 : 40 wt). For reference measurements, cells containing the commercial electrolyte LP40 as well as an electrolyte composed of 1 m $LiPF_6$ in EC : PC (50 : 50 wt), *i.e.*, without linear carbonates, were prepared and tested under identical conditions. Following the formation procedure, all cells were charged to a fully charged state (100% state of charge). During the HWS experiments, the cell temperature was increased stepwise in increments of 5 °C. Each heating step was followed by a 20 min (quasi-)adiabatic hold to allow detection of potential self-heating behavior in the absence of external energy input. The onset of self-heating indicates exothermic processes occurring inside the cell.

Fig. 14 compares the thermal response of NCM/graphite cells containing the different electrolyte systems under HWS conditions. For all investigated cells, pronounced exothermic reactions are observed at temperatures of approximately 175 °C, which can be attributed to the onset of cathode decomposition and associated reactions.[50–52] These processes represent a common high-temperature failure mechanism, primarily driven by cathode decomposition, with the electrolyte formulation influencing the onset and severity of the exothermic reactions.[53]

At lower temperatures, however, clear differences between the electrolyte systems become apparent. Cells containing $LiPF_6$-based electrolytes, including both LP40 (Fig. 14(a)) and the EC:PC formulation without linear carbonates (Fig. 14(b)), exhibit an earlier onset of self-sustained temperature increase at around 110 °C. This behavior indicates the occurrence of exothermic reactions well below the cathode decomposition temperature and is typically associated with the thermal instability and decomposition of the SEI, which acts as a primary trigger for thermal runaway.[50,53] Once initiated, this self-heating proceeds without external energy input, thereby posing a significant safety risk.

In contrast, the cell employing the LiBOB–DMA-based electrolyte (Fig. 14(c)) does not show any self-sustained exothermic behavior in this lower temperature regime. The absence of measurable self-heating up to substantially higher temperatures demonstrates a delayed onset of electrolyte-driven exothermic reactions. This behavior highlights the improved

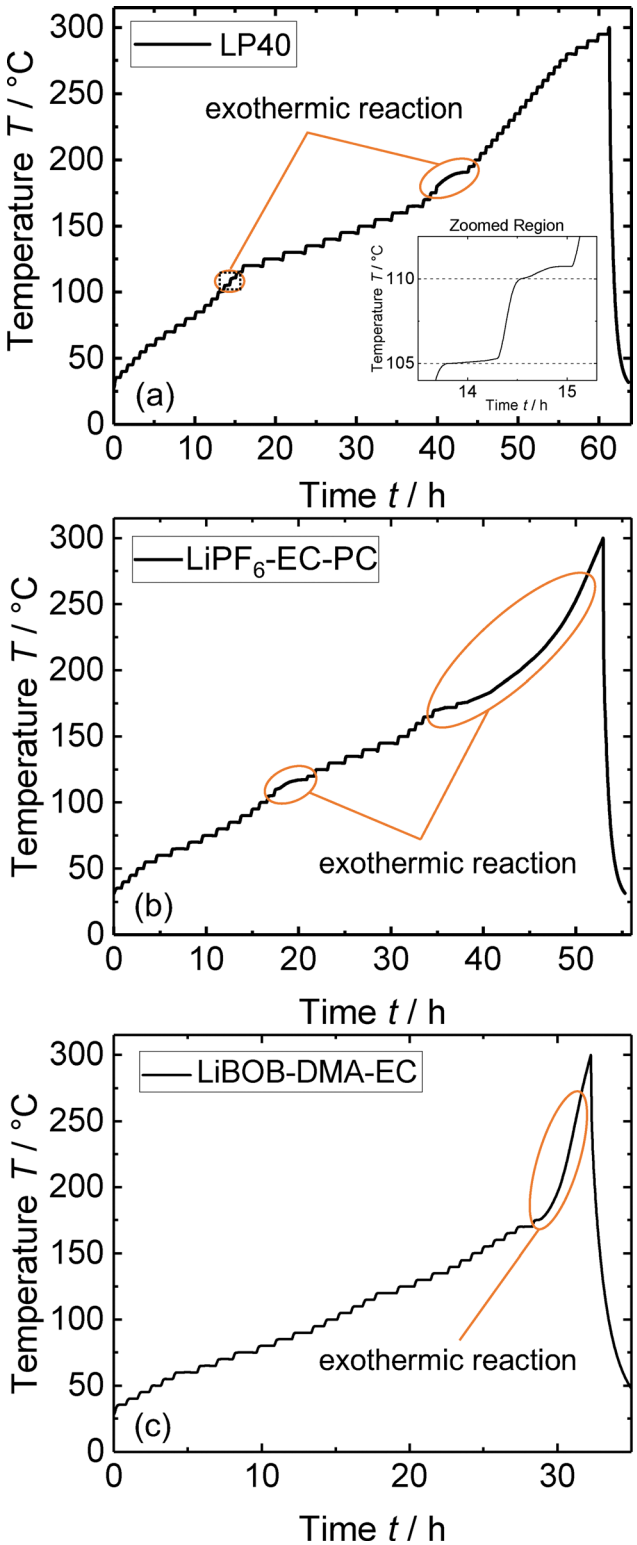

Fig. 14 Thermal abuse behavior of NCM/graphite cells containing (a) LP40 (b) 1 m $LiPF_6$ in EC : PC (50 : 50 wt) and (c) 0.7 m LiBOB in DMA : EC (60 : 40 wt). All cells exhibit exothermic reactions starting at approximately 175 °C. In addition, cells containing $LiPF_6$-based electrolytes show an earlier onset of a self-sustained temperature increase at approximately 110 °C.

intrinsic thermal stability of the LiBOB–DMA electrolyte system and results in a significantly enlarged safety margin against thermally induced failure compared to conventional $LiPF_6$-based electrolytes.

4 Conclusion

In this work, a fluorine-free electrolyte system based on the solvent DMA and the lithium salt LiBOB, optimized for NCM/graphite lithium-ion cells, was developed and systematically evaluated with respect to electrochemical performance, physicochemical properties, thermal stability, and safety-relevant properties. By combining DMA with suitable co-solvents (EC and PC) and deliberately avoiding linear carbonates, electrolytes with sufficient ionic conductivity over a wide temperature range were obtained, despite the intrinsically higher viscosity of the ester-based solvent system. Compared to LP40, the DMA-based electrolyte exhibits an approximately twofold higher viscosity and an ionic conductivity reduced by a factor of two to three. This lower conductivity contributes to increased polarization and explains the slightly reduced initial usable capacities observed at 10 and 25 °C. Nevertheless, the achieved conductivity remains sufficient for stable cell operation, and this initial limitation is more than compensated by the markedly improved cycling stability of the LiBOB–DMA-based electrolytes. At 25 °C, the cell containing 0.7 m LiBOB in DMA : EC (60 : 40 wt) electrolyte demonstrates superior long-term cycling stability compared to LP40, retaining over 80% of its initial post-formation capacity after 1000 cycles. In contrast, LP40 retains only about 50%, with the capacity curves crossing after approximately 400 cycles. The faster degradation of LP40 may be associated with the limited chemical stability of $LiPF_6$-based carbonate electrolytes. The detection of POF_3-related decomposition products by GC is consistent with $LiPF_6$ degradation pathways, which could contribute to interfacial side reactions and impedance growth during prolonged cycling.[54] At elevated temperatures (40–60 °C), the LiBOB–DMA-based cells deliver higher discharge capacities from the outset and show substantially slower degradation than LP40. While the LiBOB–DMA cells do experience somewhat faster degradation at elevated temperatures compared to 25 °C, the increase is much less pronounced than for LP40. In particular, at 60 °C, LP40 cells retain only about 40% of their initial capacity after 240 cycles, whereas the LiBOB–DMA cells still maintain over 70%, highlighting the pronounced high-temperature stability of the DMA-based electrolyte system.

DSC measurements further confirmed the improved thermal stability of the LiBOB–DMA-based electrolyte, with decomposition-related thermal events shifted to significantly higher temperatures compared to LP40. While the higher glass transition temperature indicates reduced low-temperature ion mobility, the comparable liquidus temperatures demonstrate the suitability of the DMA-based electrolyte for practical operating conditions.

Safety-relevant investigations further emphasize the advantages of the LiBOB–DMA-based electrolyte. The flash point of the DMA : EC (60 : 40 wt) solvent mixture is 135 °C, nearly 100 K higher than that of the conventional carbonate-based reference electrolyte LP40, thereby providing a substantially enlarged safety margin under abusive thermal conditions. Heat–wait–seek tests in an ARC reveal that cells with $LiPF_6$-based electrolytes initiate exothermic self-heating reactions at temperatures around 110 °C, which can be assigned to SEI decomposition. In contrast, no such early self-heating is observed for the LiBOB–DMA-based electrolyte, with exothermic reactions occurring only at higher temperatures in the range of cathode decomposition.

Overall, the results demonstrate that the LiBOB–DMA electrolyte system offers a compelling combination of enhanced thermal safety, high electrochemical stability, and long-term cycling performance. These findings underscore the potential of DMA-based, fluorine-free electrolytes as viable alternatives to conventional $LiPF_6$-carbonate-based systems, particularly for lithium-ion batteries intended for operation under elevated temperatures or increased safety requirements.

Author contributions

Larissa Kiefer: conceptualization, methodology, project administration, investigation, data curation, formal analysis, visualization, writing - original draft. Chengwen Bo: investigation, formal analysis, writing – review & editing. Philipp Finster: methodology, investigation, data curation, formal analysis, writing – review & editing. Carlos Ziebert: methodology, resources, writing – review & editing. Andreas Hofmann: methodology, resources, investigation, data curation, formal analysis, writing - review & editing. Meichen Zhan: methodology, investigation, writing - review & editing. Kai Peter Birke: conceptualization, funding acquisition, resources, supervision, writing – review & editing. All authors have read and agreed to the published version of the manuscript.

Conflicts of interest

The authors declare no conflict of interest. The funders had no role in the design of the study; in the collection, analysis, or interpretation of data; in the writing of the manuscript, or in the decision to publish the results.

Data availability

All relevant data supporting the findings of this study are included in the article. Additional data, including raw measurement data, are available from the corresponding author upon reasonable request.

Acknowledgements

This research was funded by the Bundesministerium für Wirtschaft und Energie within the Klebbatterie – Entwicklung einer Festkörperbatterie auf Basis eines aufgesprühten klebenden Elektrolyten project (03EI6102C). The authors thank

Münster Electrochemical Energy Technology for providing the NCM622 electrode material and Varta AG for providing the graphite and NCM622 electrode material.

References

1 P. Isken, C. Dippel, R. Schmitz, R. Schmitz, M. Kunze, S. Passerini, M. Winter and A. Lex-Balducci, *Electrochim. Acta*, 2011, **56**, 7530–7535.
2 T. M. Bandhauer, S. Garimella and T. F. Fuller, *J. Electrochem. Soc.*, 2011, **158**, R1.
3 H. Xiang, H. Wang, C. Chen, X. Ge, S. Guo, J. Sun and W. Hu, *J. Power Sources*, 2009, **191**, 575–581.
4 K. Xu, *Chem. Rev.*, 2014, **114**, 11503–11618.
5 Z. Zeng, B. Wu, L. Xiao, X. Jiang, Y. Chen, X. Ai, H. Yang and Y. Cao, *J. Power Sources*, 2015, **279**, 6–12.
6 K. Xu, *Chem. Rev.*, 2004, **104**, 4303–4418.
7 N. P. Pieczonka, L. Yang, M. P. Balogh, B. R. Powell, K. Chemelewski, A. Manthiram, S. A. Krachkovskiy, G. R. Goward, M. Liu and J.-H. Kim, *J. Phys. Chem. C*, 2013, **117**, 22603–22612.
8 C. L. Campion, W. Li and B. L. Lucht, *J. Electrochem. Soc.*, 2005, **152**, A2327.
9 O. Bushkova, T. Yaroslavtseva and Y. A. Dobrovolsky, *Russ. J. Electrochem.*, 2017, **53**, 677–699.
10 F. Zeng, X. Tong, C. Xu, Z. Li and Z. Liu, *ACS Omega*, 2025, **10**, 47455–47470.
11 K. Xu, S. Zhang, B. A. Poese and T. R. Jow, *Electrochem. Solid-State Lett.*, 2002, **5**, A259.
12 L. Larush-Asraf, M. Biton, H. Teller, E. Zinigrad and D. Aurbach, *J. Power Sources*, 2007, **174**, 400–407.
13 Z. Xiao, J. Liu, G. Fan, M. Yu, J. Liu, X. Gou, M. Yuan and F. Cheng, *Mater. Chem. Front.*, 2020, **4**, 1689–1696.
14 F. Wu, A. Mullaliu, T. Diemant, D. Stepien, T. N. Parac-Vogt, J.-K. Kim, D. Bresser, G.-T. Kim and S. Passerini, *InfoMat*, 2023, **5**, e12462.
15 Y. Liu, X. Wen, T. Huang and A. Yu, *J. Power Sources*, 2024, **623**, 235398.
16 S. Mardi, A. J. Naylor, J. Mindemark and G. Hernández, *J. Mater. Chem. A*, 2025, **13**, 39903–39914.
17 Z. Lu, T. Patranika, A. J. Naylor, J. Mindemark, S. Tardif, G. Hernández and S. Lyonnard, *Small*, 2025, **21**, 2410654.
18 X. Cui, F. Tang, Y. Zhang, C. Li, D. Zhao, F. Zhou, S. Li and H. Feng, *Electrochim. Acta*, 2018, **273**, 191–199.
19 P. Wang, H. Qing, R. Zhang and W. Li, *npj Mater. Sustainability*, 2025, **3**, 32.
20 G. Hernández, R. Mogensen, R. Younesi and J. Mindemark, *Batteries Supercaps*, 2022, **5**, e202100373.
21 C. Limachi, K. Rogala, M. Broszkiewicz, M. Cabello, L. Niedzicki, M. Armand and W. Wieczorek, *Molecules*, 2024, **29**, 4698.
22 F. Azeez and P. S. Fedkiw, *J. Power Sources*, 2010, **195**, 7627–7633.
23 A. Hofmann, Z. Wang and T. Hanemann, *J. Appl. Electrochem.*, 2026, **56**, 112.
24 L. Kiefer, M. Ströbel, P. Finster, C. Ziebert and K. P. Birke, *J. Electrochem. Soc.*, 2025, **172**, 120505.
25 E. Ince, *Fluid Phase Equilib.*, 2005, **230**, 58–63.
26 M.-J. Lee, C.-H. Lai, T.-B. Wang and H.-M. Lin, *J. Chem. Eng. Data*, 2007, **52**, 1291–1296.
27 *Dimethyl adipate | 627-93-0*, https://www.chemicalbook.com/ProductChemicalPropertiesCB1412954_EN.htm, 2026, Accessed: 2026-01-15.
28 Institut für Arbeitsschutz der Deutschen Gesetzlichen Unfallversicherung (IFA), GESTIS-Stoffdatenbank: Dimethyladipat (CAS 627-93-0), https://gestis.dguv.de/data?name=032130, 2026, Accessed: 2026-01-15.
29 J. C. Diogo, F. J. Caetano and J. M. Fareleira, *Fluid Phase Equilib.*, 2014, **367**, 85–94.
30 Sigma-Aldrich, *Dimethyl adipate, Product No. 186252*, https://www.sigmaaldrich.com/DE/de/product/aldrich/186252, 2026, Accessed: 2026-01-15.
31 S. Hess, M. Wohlfahrt-Mehrens and M. Wachtler, *J. Electrochem. Soc.*, 2015, **162**, A3084.
32 P. Kurzweil and O. K. Dietlmeier, *Elektrochemische Speicher*, Springer, 2018.
33 Institut für Arbeitsschutz der Deutschen Gesetzlichen Unfallversicherung (IFA), *GESTIS-Stoffdatenbank: Ethylencarbonat (Ethylene carbonate, ZVG 490120, CAS 96-49-1)*, https://gestis.dguv.de/data?name=490120, 2026, Accessed: 2026-01-15.
34 Institut für Arbeitsschutz der Deutschen Gesetzlichen Unfallversicherung (IFA), *GESTIS-Stoffdatenbank: Propylencarbonat (Propylene carbonate, ZVG 070730, CAS 108-32-7)*, https://gestis.dguv.de/data?name=070730, 2026, Accessed: 2026-01-15.
35 Institut für Arbeitsschutz der Deutschen Gesetzlichen Unfallversicherung (IFA), *GESTIS-Stoffdatenbank: Diethylcarbonat (Diethyl carbonate, ZVG 023150, CAS 105-58-8)*, https://gestis.dguv.de/data?name=023150, 2026, Accessed: 2026-01-15.
36 K. Xu, S. P. Ding and T. R. Jow, *J. Electrochem. Soc.*, 1999, **146**, 4172.
37 J. Kasnatscheew, B. Streipert, S. Röser, R. Wagner, I. C. Laskovic and M. Winter, *Phys. Chem. Chem. Phys.*, 2017, **19**, 16078–16086.
38 L. Wildersinn, D. Stottmeister, F. Jeschull, A. Groß and A. Hofmann, *ACS Appl. Mater. Interfaces*, 2025, **17**, 10055–10072.
39 S. Ding, K. Xu, S. Zhang, T. Jow, K. Amine and G. Henriksen, *J. Electrochem. Soc.*, 1999, **146**, 3974–3980.
40 G. W. H. Höhne, W. Hemminger, H.-J. Flammersheim *et al.*, *Differential scanning calorimetry*, Springer, 2003, vol. 2.
41 S. Klick, P. Finster, K. M. Graff, C. Ziebert, G. Stahl, F. Weber, E. Figgemeier and D. U. Sauer, *EES batteries*, 2026, **2**, 1023–1039.
42 A. Hofmann, M. Migeot, E. Thißen, M. Schulz, R. Heinzmann, S. Indris, T. Bergfeldt, B. Lei, C. Ziebert and T. Hanemann, *ChemSusChem*, 2015, **8**, 1892–1900.
43 I. U. Mohsin, C. Ziebert, M. Rohde and H. J. Seifert, *J. Electrochem. Soc.*, 2021, **168**, 050544.
44 C. Ziebert, A. Melcher, B. Lei, W. Zhao, M. Rohde and H. Seifert, *Emerging Nanotechnologies in Rechargeable Energy Storage Systems*, Elsevier, 2017, pp. 195–229.
45 Y.-P. Yang, A.-C. Huang, Y. Tang, Y.-C. Liu, Z.-H. Wu, H.-L. Zhou, Z.-P. Li, C.-M. Shu, J.-C. Jiang and Z.-X. Xing, *Polymers*, 2021, **13**, 707.

46 R. Korthauer, *Handbuch Lithium-Ionen-Batterien*, Springer Berlin Heidelberg, Berlin, Heidelberg, 1st edn, 2013.
47 B.-T. Yu, W.-H. Qiu, F.-S. Li and L. Cheng, *J. Power Sources*, 2007, **166**, 499–502.
48 K. Xu, S. Zhang and T. R. Jow, *Electrochem. Solid-State Lett.*, 2003, **6**, A117–A120.
49 E. Zinigrad, L. Larush-Asraf, G. Salitra, M. Sprecher and D. Aurbach, *Thermochim. Acta*, 2007, **457**, 64–69.
50 B. Cui, Z. Xiao, S. Cui, S. Liu, X. Gao and G. Li, *Electrochem. Energy Rev.*, 2024, **7**, 27.
51 Y. Dai and A. Panahi, *Next Energy*, 2025, **6**, 100186.
52 D. Patel, J. B. Robinson, S. Ball, D. J. Brett and P. R. Shearing, *J. Electrochem. Soc.*, 2020, **167**, 090511.
53 Y. Yang, Y. Gao, Y. Miao, Y. Liang and X. Ren, *Batteries*, 2025, **11**, 373.
54 S. Solchenbach, M. Metzger, M. Egawa, H. Beyer and H. A. Gasteiger, *J. Electrochem. Soc.*, 2018, **165**, A3022–A3028.